Assimilation of Images

Arthur Vidard, Olivier Titaud

OXFORD
UNIVERSITY PRESS

Contents

1
Assimilation of Images

Arthur Vidard and Olivier Titaud

1.1 Motivations

Since the end of the seventies, many satellites have been launched to improve our knowledge of the atmosphere and of the oceans by observing the Earth. The geostationary ones provide photographic images of the earth system among other data. They provide sequences of such images that show the dynamical evolution of certain meteorological or oceanic "objects": fronts, clouds, eddies, vortices, etc. Dynamics that the human vision can easily detect in this kind of image sequence clearly has a strong predictive potential (Fig 1.1). This aspect is clearly favoured by the fact that these data, contrary to many other measurements, are dense in space with a resolution close to one kilometre and in time with a full image every 15mn for current METEOSAT satellites and every 10mn (and even every 2.5mn for Europe only) for the upcoming third generation. It implies a huge amount of data which can be seen as an asset but also induce difficulties for the assimilation system for coping with such amount of data. In practice only a tiny percentage ($\approx 3-5\%$) of total satellite (from polar orbiting and geostationary) data are used in operational NWP systems and images are only used through pseudo observation (see later) and given low confidence within the assimilation systems. Considering the cost of the satellite observing systems (the cost of the launch of the Meteosat Third Generation is estimated at around 2.5 billion Euros) and of the infrastructures required for the collect of the data itself, improving their impact on forecasting systems is an important topic of research.

The purpose of this section is therefore to present a brief introduction to image sequences assimilation in a geophysical context. As said before, this is still a topic of research and only basic options are used in operational systems. In relation, two classes of image assimilation techniques can be considered:

- Pseudo-Observation: an apparent velocity field is estimated from an image sequence using certain image processing techniques. This estimated field can then be used as indirect observations in a classical assimilation scheme. This is what is currently done in a meteorological context (Schmetz *et al.*, 1993).
- Direct Image Assimilation (DIA): images or image sequences are assimilated through an appropriate observation operator directly into the Data Assimilation System. This idea follows a general trend to avoid pre-processing of observations before its assimilation. This is not yet used operationally and a selection of possible metrics is presented.

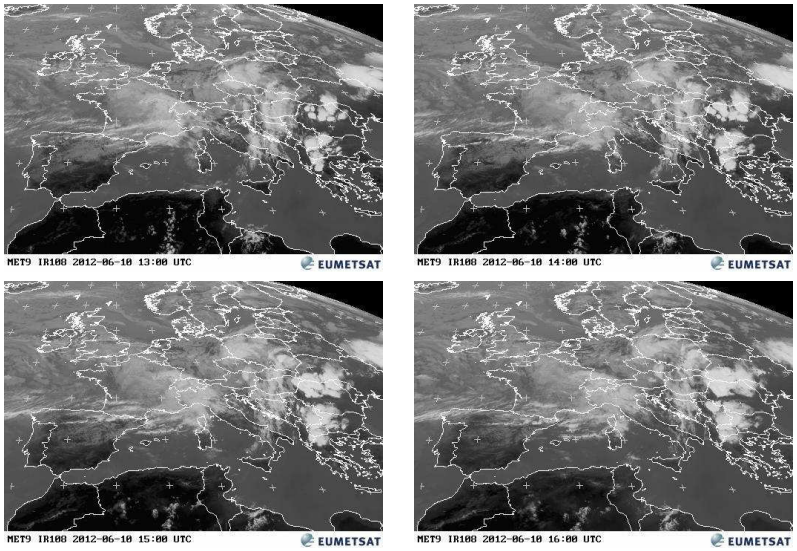

Fig. 1.1 sequence of Meteosat images over Europe the 12^{th} of june 2010 between 13:00 and 16:00 UTC (source Eumetsat)

Using images or image sequences together with numerical models may present several difficulties: First the state variables of the numerical models (e.g. wind, temperature, pressure, humidity in atmosphere modelling and current velocities, temperature, surface elevation, salinity in ocean modelling) are not directly measured by satellites. What is observed is more or less linked to those variables by diagnostic equations that will have to be included in the assimilation procedure. Moreover, the physical processes that are observed are not always taken into account in the model (e.g. local convection in atmospheric modelling, ocean colour in ocean modelling). These two aspects are not specific to images and may happen for other kinds of observation as well but they are likely to be systematic in the case of image sequences.

More specifically, images are bidimensional informations whereas physical processes of geophysical fluids are three-dimensional. From this point of view, a major difference between the ocean and the atmosphere comes from their radiative properties. In the first case images give informations about the ocean surface whereas in the second case images integrate all the radiative profile of the observed atmosphere column. Besides, certain meteorological structures (e.g. some kind of clouds) are located in specific layers. Assimilating informations about the dynamical evolution of these structures needs additional informations about the altitude of the observed processes (using temperature profile measurements for instance). When the radiative properties of the ocean make the images give information about the ocean surface only (typically about a few centimetres, up to a few meters in some cases), the corresponding observed processes may not be well depicted by the model. Additionally satellite Images can be of relatively poor quality, this is mostly true for ocean surface images very often partially occulted by clouds. Moreover they are most of the time composite images: it takes

Meteosat 15 mn to take a whole image chunk after chunk and the surface SST images come from polar orbiting satellites and could take a few days for full covering a given area (Fig 1.2). In a sequence, the luminosity of individual images in a sequence may vary according to the time of the day and only apparent motion is observed that could lead to aliasing problems. Another specificity of images is that, as for human vision, we can presume that the pertinent informations coming from an image are mainly brought by its discontinuities or high gradients. Unfortunately, numerical models have a tendency to smooth these discontinuities out.

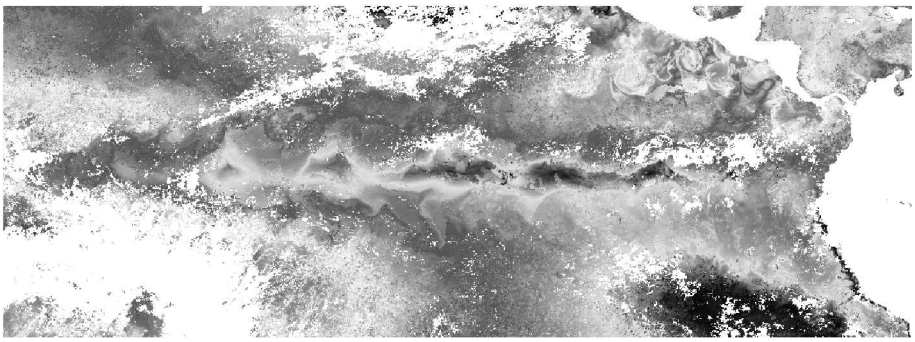

Fig. 1.2 Infra red composite image from Metop 21^{st} of January 2008 (source Ifremer)

Finally, as aforementioned handling the massive amount of data included in an image sequence is particularly challenging

In order to tackle the above-mentioned difficulties, one has to carefully design the assimilation system. It should be able despite these difficult conditions to extract from the observations the information about the dynamics of the system. The difficulty in building such system lies in the adequate definition of the observation space and the related metrics and consequently through the construction of the observation operator.

1.2 Images: Level(s) of Interpretation

Before really considering the assimilation of images, let us better define what an image is in this context. For the human eyes it is structured information, dense on the domain it covers; for a computer it is an array of pixels and from a mathematical point of view... it can be many things.

But basically an image is considered as a function of two variables

$$\begin{aligned} I : \Omega \subset \mathbb{R} \times \mathbb{R} &\to \mathbb{R} \\ (x, y) &\mapsto f(x, y) \end{aligned} \tag{1.1}$$

whose definition can be of very different nature (see section 1.2.3)

1.2.1 Numerical raw images

The acquisition device converts the radiations coming from the observed scene into an electric signal that is digitalised to form the *raw image*. A numerical raw image is

an array of pixels whose values represent the quantity of photons the corresponding photo-site received during the acquisition procedure. Raw images pixels can then be considered as radiance measurements. However, from a *mathematical* point of view, an image is commonly considered as a real valued function of two continuous real variables. This allows the use of powerful mathematical tools developed by the image processing scientific community. A *numerical image* is the discrete version of a mathematical one that is finally manipulated by computers.

1.2.2 Levels of interpretation

An image can be considered at different level of interpretation:

At the *pixel level*, an image of a fluid in motion is a digital instantaneous expression of the state of the fluid through the radiation that it reflects (visible light) or emits (infrared light). It is then a snapshot of an *apparent state*, which may involve other physical quantities than what the model simulates, like tracers (e.g. Cloud cover and aerosols in the atmosphere, chlorophyll in the ocean). The radiances are generally not part of the studied system and the dependence between this radiation and the state variables is not often trivial. For instance, *cloud cover* is an intricate function of the state variable of meteorological models: clouds reflectance and intrinsic infrared emission depend both on thermodynamics (temperature and humidity) and on the micro-physical processes that occur inside the clouds (involving water, ice, snow and the size of the particles). At this level, information contained in images is not structured and represents a huge amount of data: typical satellite images are about 5000×5000 size, that is 25 millions of pixels. This number should be multiplied by the number of frames in the observed sequence.

At the *analysis level(s)*, an image is symbolically described by its contents, typically by the objects and their characterisation (geometry, layout, etc.) that appear in the observed scene or on its mathematical description (see further). This kind of interpretation is used for high-level vision problematics as motion estimation, edge detection, pattern recognition, etc. The advantage of this level is that it may less depend on the effective radiance emission and it allows emphasising on the structures the image contains (and even their evolution in an image sequence) rather than the actual value of individual pixels.

A good illustration of these different levels of interpretation is the two images from two different MODIS sensor shown in figure 1.3. At pixel level they represent two very different and somewhat independent quantities of very different nature (Temperature and Chlorophyll) while at a higher level of interpretation, both images give a similar kind of information about the dynamic of the system. Indeed, one can easily notice the vortices and fronts that are present in the images.

1.2.3 Mathematical definition

There exist several mathematical definitions for images and it is not the aim of this section to describe them all and only a small subset will be discussed in the following. They essentially depend on the way the image needs to be processed. We can cite the multi-scale decomposition approach which comes from the signal processing theory (*wavelet* (Mallat, 1998) and the more recent *curvelet* (Candès and Donoho,

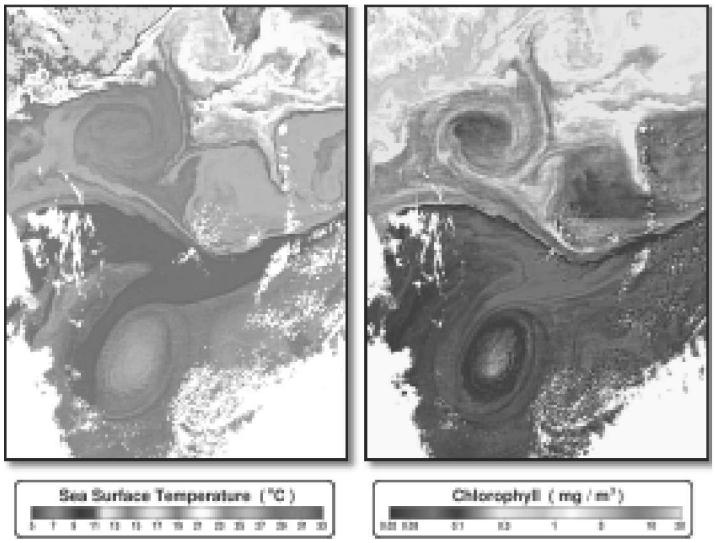

Fig. 1.3 Images over the Gulf Stream the 4^{th} of August 2005 from Aqua satellite (MODIS radiometer). Ocean Sea Surface Temperature (IR channel, left) and chlorophyll concentration (visible channel, right). (Source : NASA)

2003) transforms). Another approach uses the Partial Differential Equation framework (Aubert and KornProbst, 2006) where the image is considered as a function of two variables verifying a PDE equation that depends on the considered image-processing problem. Certain applications use a stochastic approach as well to define images as a combination of an "ideal" image (most often deterministic) and a random function (Geman and Geman, 1984). For a good review of image analysis and the underlying mathematical definition, see (Chan and Shen, 2005).

In the DA framework, the level of interpretation together with the mathematical definition of the image may be represented by the image-type observation space and its corresponding observation operator (see Section 1.4).

1.3 Current Use of Images in DA: Pseudo Observation

Sequences of images are widely available in meteorology, oceanography, hydrology, astrophysics, and even medicine. Historically, they have been mainly used for a "by eye" analysis from experts in these fields. Yet, since the mid 80's, research has been carried out to derive velocity fields from the sequences, with applications for fluid dynamics mainly (and very recently for movie compression and medical applications). One way to assimilate images is to use the velocity field derived from some image processing techniques as pseudo-observation of the studied system. This class of Motion Estimator, directly based on image processing techniques, aims at estimating the velocity field that would "transport" one frame to another or one part of the frame to the other frame.

There are several ways to extract a velocity field from a sequence of images. They are mainly working on two successive frames, even though some extensions allow for the use of more frames at the same time. Hereafter is a short list of the most common methods.

1.3.1 Bogus

The simplest method to assimilate images is to detect specific features in the images and add or displace them in the system. Historically both steps of this process were done manually by forecasters and modellers, but recently some effort has been carried out to do the detection automatically, like for instance with the dry intrusions that are important precursor of extreme event (see figure 1.4 and Michel and Bouttier (2006)) as well as for the assimilation itself *e.g.* with the use of pseudo observation of potential vorticity structures Michel (2011).

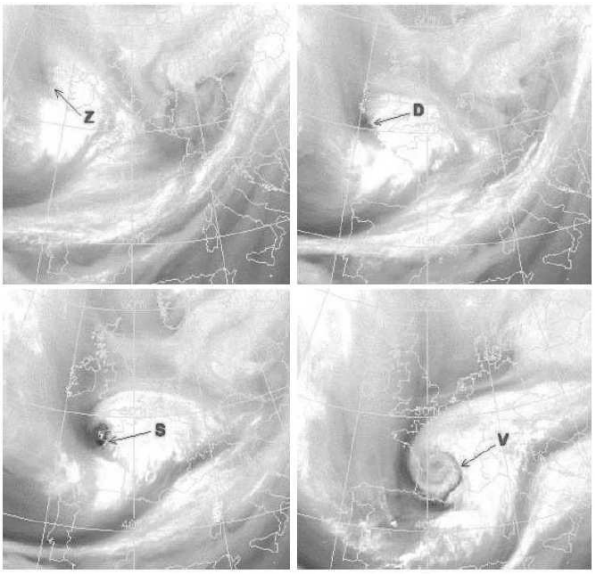

Fig. 1.4 Evolution of a dry intrusion (source Météo-France)

1.3.2 Statistical methods

They were set up for Particle Image Velocities (PIV) and Particle Tracking Velocities (PTV) experiments i.e. for lab experiments in fluid mechanics where particles are added to the fluid in order to follow the flow (Adrian, 1991). In this kind of method two successive images are divided into small areas and cross-correlation techniques can be used to match each individual areas of the first image with one of the second image.

$$C = \frac{\sum_{i,j}(T_1(i,j) - \bar{T_1})(T_2(i,j) - \bar{T_2})}{\sigma_{T_1}\sigma_{T_2}} \tag{1.2}$$

with T_1 and T_2 represent the spatial distribution of grey values in the first and second image templates, respectively. The T_2 corresponding to the highest C is elected (if C is larger that a given threshold, typically 0.8).

It is then possible to create a velocity field that would transport all the areas of the first image to the second one. They are easy to implement, but they can be quite expensive when the number of areas increases. Since the resulting velocity vectors are based on cross-correlating the intensity distributions over small areas of the flow, the resulting velocity field is a spatially averaged representation of the actual velocity field. This obviously has consequences for the accuracy of spatial derivatives of the velocity field, vorticity, and spatial correlation functions that are often derived from PIV velocity fields. PIV methods will obviously not be able to measure vertical velocities. These components might not only be missed, they can also induce errors in the estimated horizontal velocity fields. There also exist Stereoscopic PIV, which uses two cameras to estimate all three velocity components (if the observed media allows for it) but they are for obvious practical reason only available for laboratory experiment for now.

This is the kind of method that is actually currently used in NWP to derive winds from the satellite images from geostationary satellite (METEOSAT, GOES and GMS), with the so-called AMV (Atmospheric Motion Vectors). The clouds are used in this process instead of the particles in classical PIV methods and due to the peculiar nature of these tracers the images require two pre-processing steps prior to the wind estimations. First, since the tracers (clouds) are not uniformly spread across the image one has to detect, in each area, features of interest that would be tracked from one image to another with methods generally based on the gradient of the images. A lot of quality control procedures are then applied to the selected features to retain only those that will be traceable. For instance, the gradients have to be large enough, cover a significant portion of the area, avoid areas more than two different gradient amplitude, etc.

Second, images are 2D representations of a 3D system and therefore one has to allocate a height at a given tracked feature (with the reasonable assumption that clouds will not move up and down between two images). Historically (and still used as a fallback) the window channel brightness temperatures within the target area were analysed, and a mean value for the coldest 20% of the sample was used to represent the temperature at cloud top. This temperature was then compared to a numerical forecast of the vertical temperature profile to arrive at the height of the cloud. More recently AMV producers use the so called CO_2 Slicing where the ratio of the IR and CO_2 absorption can be linked to the pressure at the location of the observed feature or the H_2O intercept that uses the fact that the radiances from a single-level cloud deck for two spectral bands vary linearly with cloud amount. Both CO_2 slicing and H_2O intercept require a model forecast for calibration. This step is an important source of errors in the derivation of AMVs, moreover these errors are correlated with the model error since a model forecast is used in the processes. This last aspect is an important breach of the common assumption of uncorrelated errors between model and observation that is made by all the main data assimilation algorithms.

Once this is done PIV methods can be used to derive wind fields on several altitudes. In order to avoid too much noise in the resulting wind field three images are

used instead of two to derive 2 wind fields (from image 1 to 2 and from a image 2 to 3) and only the sum of the resulting vectors that do not disagree are kept for the final product. (a complete description of these processes can be found in Schmetz *et al.* (1993) and Nieman *et al.* (1997)).

Due to their really indirect nature and the complexity of the pre and post processing, describing the errors associated to such wind data is not straight forward, in particular they are correlated so complex observation error covariance matrices have to be built or the errors have to be significantly inflated, and therefore it will reduce their impact. Bormann *et al.* (2003) found statistically significant spatial error correlations on scales up to about 800 km, and moreover they are strongly anisotropic.

1.3.3 Optical flow

Variational methods are probably more adapted to the treatment of the large image sequences available in geophysics even though they are seldom used in practice. The most common one is usually called *optical flow*. This classical approach in computer vision is based on the conservation of the global luminance between two images (Horn and Schunck, 1981) and they aim at finding the velocity field $\mathbf{w} = (u, v)$ that transport two successive images I_1 and I_2 one to another.

$$I_1(x + u(x, y), y + v(x, y)) = I_0(x, y) \tag{1.3}$$

A vector field satisfying this equation is not unique (aperture problem) and a strict conservation is not realistic in general. So it is transformed into a minimisation problem:

$$J(\mathbf{v}) = \frac{1}{2} \int \|I_1(x + u(x, y), y + v(x, y)) - I_0(x, y)\|^2 dxdy + \frac{1}{2}\alpha R(u, v) \tag{1.4}$$

The choice of the regularisation term depends on the application field (Vigan *et al.* (2000) for oceanography, Amodei and Benbourhim (1991) for wind field). A good review of possible R in available in Auroux and Fehrenbach (2010) and some thoughts about preconditioning in Souopgui (2010). The advantage of such method over PIV is that it can provide a denser velocity field for a fraction of the computing cost (see Figure 1.5) however the adjustment or the relative weight of the two terms of the cost function (*i.e.* the value of the parameter α) and the choice of the regularisation term are far from trivial (Souopgui, 2010).

Once again this motion estimator is meant to be used for a pair of images, however as for statistical (but in a more natural manner) it can be extended to use more frames altogether in order to improve consistency, by adding a governing equation for $\mathbf{v}$ to the optimality system generating the pseudo observations.

As above, it assumes the conservation of light and the image pixels are transported from one image to the other by the velocity field to be estimated. In order to improve the temporal consistency of the estimated velocities, this method requires a simple temporal evolution model $\mathcal{N}$. Along with the transport equation of the pixels (1.4) it forms:

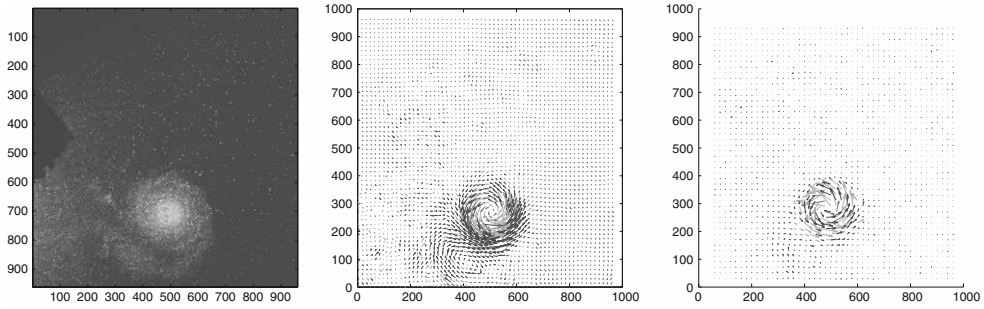

Fig. 1.5 From left to right: First original image, velocity field derived from optical flow, velocity field derived from PIV. Light, medium and dark: high, medium and low confidence respectively (from Auroux and Fehrenbach, 2010)

$$\begin{cases} \dfrac{\partial I}{\partial t} + \nabla I \cdot \mathbf{v} = 0, \\ \dfrac{\partial \mathbf{v}}{\partial t} = \mathcal{N}(\mathbf{v}), \quad I(0) = I_0, \quad \mathbf{v}(0) = \mathbf{v}_0. \end{cases} \tag{1.5}$$

The pixel values of the images I_{obs} are then assimilated in the previous model using variational data assimilation (see Section 2.1) where the control variable is the initial condition $\mathbf{v}_0$ of $\mathcal{N}$.

$$J(\mathbf{v}) = \frac{1}{2} \sum_{i=1}^{m-1} \int \|I_i(x + u(x,y), y + v(x,y)) - I_{i-1}(x,y)\|^2 dxdy + \frac{1}{2}\alpha R(u,v) \tag{1.6}$$

The advantage of this approach is that it takes into account all the images of the sequence at once and therefore can cope with missing data on some of the frames. This has been applied, using a constant velocity ($\mathcal{N} = 0$) in (Korotaev *et al.*, 2008) to derive ocean surface velocity fields from SST on the Black Sea.

1.3.4 Advantages and limitations of the pseudo-observation technique

The main advantage of such approach is simplicity; indeed, even though the algorithm use to produce pseudo velocity observations may be sophisticated, the use of the pseudo observation in an already existing DA scheme is relatively straightforward. There is no issue of differentiation and no heavy development is generally needed since this processing is done off-line.

However, despite their relative simplicity for implementation and their rapidity, pseudo-observation techniques based on motion estimation may suffer from some limitations. First, a frame-to-frame motion estimator does not take into account a sequence of more than two images. Due to the lack of consistency in time, it cannot capture the dynamical evolution of the image during the entire assimilation window. One of the consequences is that it cannot deal with missing data, which can be quite frequent in some of the applications targeted here. Missing data can be due to a glitch in the

observing system or an obstacle (e.g. clouds). Solving 1.6 may mitigate this disadvantage, yet the model $\mathcal{N}$ of the temporal evolution of the velocity only depends on $\mathbf{v}$ and therefore is likely to be a somewhat poor representation of the real behaviour of the velocity.

Neither of these two techniques takes into account physical information about the underlying physical processes observed in the images. Furthermore some assumptions like the conservation of the luminance are clearly not valid for fluid flow images showing broken up structures. Finally, velocity fields obtained through the pseudo-observation approach are apparent velocities that can be quite different from the actual velocities. For instance, the absence of a tracer in a subset of an image sequence will lead to null apparent velocities in that area. Such techniques then need to provide error maps to account for this kind of error in the interpretation of the observation. Therefore, the definition of the observation operators and the specification of the corresponding observation error matrices are likely to be a difficult task Bormann *et al.* (2003).

For all these reason an important research effort is being carried out on that topic in order to define a methodology direct image data assimilation that would combine the information coming from image sequences and the ones coming from the numerical model, a-priori knowledge and classical observations in a more consistent way (e.g. without the need of pseudo observations).

1.4 Direct Assimilation of Images

If one wants to avoid going through the pseudo observation route the main difficulty is to define a way of measuring the discrepancy between the model outputs and the images. That is to define the observation space $\mathcal{I}$ and the associated distance $d_{\mathcal{I}} : \mathcal{I} \times \mathcal{I} \to \mathbb{R}$, and the observation operator $H : \mathcal{X} \to \mathcal{I}$. There are many ways to define this triplet from very basic to highly sophisticated. For instance, to define $\mathcal{I}$ we could consider

1. Frequency characteristics: in that case, $\mathcal{I}$ is the image space of a multi-scale transformation such as wavelet and curvelet transforms. This approach is interesting for its well-known efficiency in data compression, denoising and edge extraction.
2. Geometric characteristics: certain image analysis techniques can detect certain geometrical features in the image (e.g. by means of active contours). This feature may take the form of a parametrised curve in $\mathbb{R}^2$ which could be assimilated as Lagrangian observation. This approach will necessitate high-level image analysis.
3. Qualitative characteristics: in geophysics, there are several recognisable structures connected to physical phenomena (e.g. cyclone, front, etc.). We could define $\mathcal{I}$ as a dictionary of such couples observable structure / physical phenomenon. More specifically in meteorology, clouds may give information about the flow or the physical processes where they are located. For instance, the particular shape of the stratus clouds is due to a stratified flow whereas cumulo-nimbuses are known to involve strong convective processes.

In order to choose the above-defined triplet, one may start from the observation operator. $H_{\mathcal{I}}$ has to extracts structures from model state variables (possibly in a differentiable manner) and this can be done, either by creating a synthetic image from

the model output and then perform the same extraction on both observed image and synthetic image in order to define the observation space and its associated distance, or by directly extracting these structure from the model output.

In the following two examples of such definition are presented, one using the synthetic observations route, the second directly extracting dynamical features from the model output and matching them to the one from the images.

1.4.1 Synthetic images and multi-scale transform

Features in geophysical images such as eddies or filaments may correspond to tracers in the observed system. A tracer can be defined as any quantity that is transported by the fluid flow. For instance, potential vorticity, temperature, salinity can be considered as atmospheric and ocean tracers. Modelling and simulating their evolution from the model state variables may help to define the Structures Observation operator. Indeed, we may use their description maps (e.g. concentration maps) as a *Synthetic Image Sequence* from which comparison with images (in a sense that remain to be defined) can be performed.

In other words, if $\mathbf{q}$ is the tracer concentration, one can model its evolution by transporting it through the model velocity field using a standard transport equation:

$$\frac{\partial \mathbf{q}}{\partial t} + \nabla \mathbf{q}.\mathbf{u} = 0 \tag{1.7}$$

where $\mathbf{u}$ is the model velocity. This allow to produce a field that will be comparable to observation from the model output; once again, as for optical flow, this equation can be different, depending on the observed quantity. This way of proceeding requires the availability of the initial tracer field. It can be done thanks to an image at the beginning of the time period, but it cannot cope with missing data. Alternatively, one can augment the state vector with the concentration $\mathbf{q}$ and control its initial condition (or filter its trajectory depending on the assimilation scheme) along with the state vector's.

Yet certain features of interest in geophysical fluid images do not correspond to any tracers (such as waves or dry intrusions in atmosphere images). In that case, other techniques should be developed to extract structures from model outputs without synthetic image sequence production.

From this observation operator there are plenty of possible choices for the observation space. The simplest of them being L^2 with the classical norm: $d^2(\mathbf{x}, I) = \|H(\mathbf{x} - I\|^2_{L^2}$. In the discrete case, it means comparing the synthetic image ($H(\mathbf{x})$) to the observed one, pixel by pixel independently. Papadakis and Memin (2008) showed that assimilating pixel levels directly gives a better result than using an optical flow-based pseudo-observation approach. Also in Corpetti *et al.* (2009) such formalism is used to assimilate images of pressure differences into a three-layer simplified atmospheric model. Nevertheless, we could point out two possible limitations of the use of pixel level for realistic applications in geophysics: first for large images, the number of observation will become enormous (one per pixel) making difficult any assimilation, second it cannot differentiate errors in placement with error in amplitude of the observed/simulated features.

(a) Original image (b) Strong threshold (c) Strong scale by scale threshold

Fig. 1.6 Original image (a) and its curvelet / threshold / reconstruction product for a strong threshold applied to all the coefficients (b) or independently scale by scale (c) both retaining 10% of the coefficients in the curvet frame

This was the motivation for the approach proposed in Souopgui (2010, Titaud *et al.* (2010) and based on a multi-scale decomposition of both synthetic and observed image. In the present case a curvlet transformed was used, but similar results can be obtained using other multi scale decomposition like wavelet for instance. It actually uses the fact that any image can be decomposed as:

$$I = \mathcal{C}(I) \equiv \sum_{j,k,l} \langle \varphi_{j,k,l}, I \rangle \varphi_{j,k,l}, \tag{1.8}$$

where $(\varphi_{j,k,l})_{j,k,l}$ are the elements of the curvelet frame. The inner product $\langle ., . \rangle$ is the usual $L^2(\mathbb{R}^2)$ one. The curvelet transform is a linear isometry and then its adjoint is given by the inverse transformation (reconstruction). This is a convenient feature for practical use in variational data assimilation framework. A threshold $\mathcal{T}$ is then applied to this decomposition (only a subset of (i, j, k) terms are kept) in order to extract the dominant features of the images. Figure 1.6 shows the effect of two different thresholding techniques on the reconstruction of a cloud image. The observation becomes:

$$\mathbf{y} = \mathcal{T} \circ \mathcal{C}(I) \tag{1.9}$$

In order to compare with the model, the same transformation is applied to the synthetic image obtained from the model output

$$\mathcal{H}(\mathbf{x}) = \mathcal{T} \circ \mathcal{C}(\mathbf{q}) \tag{1.10}$$

with $\mathbf{q}$ linked to $\mathbf{x}$ by equation 1.7. Then we can define a semi norm on $\mathcal{I}$ from the term-by-term product of the curvet coefficients that survived the threshold function.

The choice of the threshold $\mathcal{T}$ is of crucial importance as shown in Souopgui (2010) and illustrated by the figure 1.7, which compare the velocity file obtained by direct image assimilation in a shallow water model of images coming from a laboratory experiment performed at the CORIOLIS turntable (as a watermark behind the vector field). This example emphasises on the robustness of the multi scale approach to noise on the data. The L^2 norm (1.7a) gives a noisy result with numerous small displacements,

which are actually artefacts of the bad quality of the observation images. On the contrary a hard threshold (1.7b, where all the curvet coefficient below a given threshold are discarded) will have the tendency to underestimate the velocity field, while using a finer threshold (1.7c where a strong threshold is applied scale by scale independently), retaining the same number of coefficients will lead to a better reconstruction of the isolated vortex, with the right amplitude and without the unwanted small currents. It has to be noted that the convergence of the minimisation using the L^2 comparison tends to be much slower than that of the curvelet based comparison. This is due to the larger amount of observation (number of pixels vs number of curvelet coefficients) and to the stronger correlation between the pixels of a same image. This leads to the degradation of the conditioning of the minimisation problem (Haben *et al.*, 2011). For longer assimilation windows, the L^2 norm based approach does not even converge whole the truncated curvelet based one still manage to find a minimum. These results are obtained using images of a relatively modest size (256×256), this problem is likely to be amplified when switching to Meteosat-type images (5000×5000).

Moreover, the use of the pixel level may then lead to some increase in the representativity error. Note that small-scale structures may be the consequence of meso-scale dynamical processes. This is particularly true for mixing tracer processes where spirals and filaments may come from the variability of meso-scale velocity field as it is clearly shown in Lehahn *et al.* (2007). In a pixel basis, those filaments are not represented as coherent structures while another mathematical modelling could avoid this problem.

Compared to the classical L^2 norm, the use of higher level of interpretation reduces significantly the size of the observation vector (typically only a few percent of the coefficients are kept). Additionally it tends to filter out small scales that cannot be represented by the model anyway.

1.4.2 Observation operators based on Lagragian Coherent Structures

Using a Synthetic Image Sequence to define a Structure Observation may be difficult because numerical advection schemes are known to smooth discontinuities out. This drawback may lead to representativeness error: observation model may not be able to represent observed image patterns. To overcome this problem, Titaud *et al.* (2011) suggest to define observation operators based on the computation of Lagrangian coherent structures of the fluid.

Lagrangian Coherent Structures (LCS) delimit regions of whirls, stretching, or contraction of tracer (Ottino, 1989). This concept is well defined for time-independent dynamic systems, where they simply correspond to stable and unstable manifolds of hyperbolic trajectories (Wiggins, 1992): contraction is observed along stable manifolds whereas unstable manifolds correspond to divergent directions along which the tracer is stretched. This concept was generalised for flows with general time dependence (particularly geophysical flows) (Haller and Yuan, 2000; Haller, 2011) and they are usually identified in a practical manner as maximising ridges of so called backward Finite-Time Lyapunov Exponents (FTLE) field (Haller, 2000; Haller, 2001; Haller, 2002; Shadden *et al.*, 2005; Mathur *et al.*, 2007). Let $\mathbf{x}(t) = \mathbf{x}(t; \mathbf{x}_0, t_0)$ be the position of a Lagrangian particle at time t, started at $\mathbf{x}_0$ at $t = t_0$ and advected by the time-dependent fluid flow $\mathbf{u}(\mathbf{x}, t)$, $\mathbf{x} \in \Omega \subset \mathbb{R}^2$, $t \in [t_0, t_0 + T]$. The *forward* FTLE $\sigma_{t_0}^{t_0+T}(\mathbf{x}_0)$

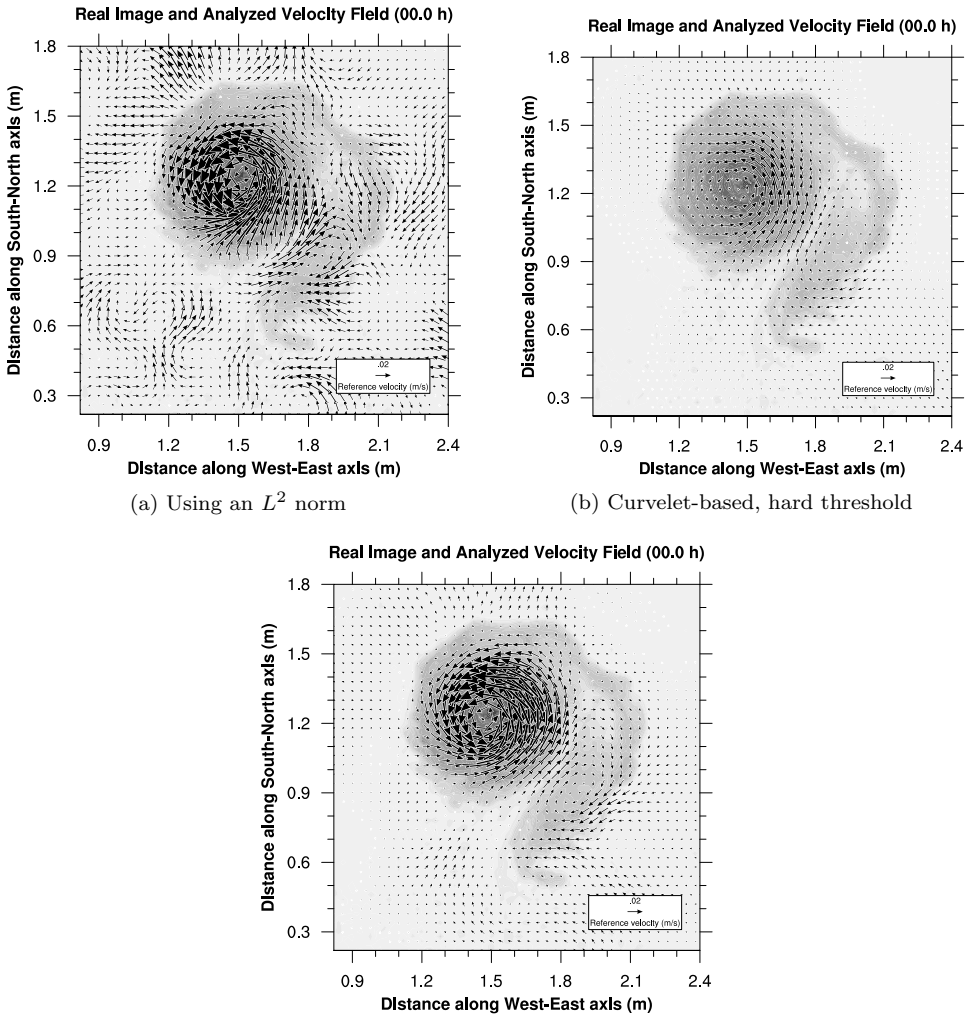

(a) Using an L^2 norm

(b) Curvelet-based, hard threshold

Fig. 1.7 Initial velocity field reconstructed by direct assimilation of a real image sequence using different observation operators and norms.

at is defined as

$$\sigma_{t_0}^{t_0+T}(\mathbf{x}_0) = \frac{1}{|T|} \ln \sqrt{\lambda_{\max}(\Delta)}, \tag{1.11}$$

where $\lambda_{\max}$ is the maximum eigenvalue of the Cauchy-Green strain tensor

$$\Delta = \left[\nabla \phi_{t_0}^{t_0+T}(\mathbf{x}_0)\right]^* \left[\nabla \phi_{t_0}^{t_0+T}(\mathbf{x}_0)\right],$$

where $\phi_{t_0}^{t_0+T}$ is the flow map of the lagrangian system. FTLE corresponds to the growth factor of the norm of a perturbation started around $\mathbf{x}_0$ and transported by the flow after the finite advection time T. The associated eigenvector $\varphi_{t_0}^{t_0+T}(\mathbf{x}_0)$ is referred to

as the *forward* Finite-Time Lyapunov Vector (FTLV): it corresponds to the direction of maximal stretching of the tracer. FTLE represents the rate of separation of initially neighbouring particles over the finite-time window $[t_0, t_0 + T]$. *Backward* FTLE-Vs are similarly defined, with the time direction being inverted in the computation of the Lagrangian trajectory. For more details on the practical computation of FTLE-V see e.g. Shadden *et al.* (2005, Shadden *et al.* (2009) and Ott (1993) for any types of flows and d'Ovidio *et al.* (2004) for oceanic flows. FTLE (FTLV) is a scalar (vector) that is computed at a given location $\mathbf{x}_0$. Seeding a domain with particules initially located on a grid leads to the computation of a discretised scalar (FTLE) and vector (FTLV) fields. Note that the FTLE-V naming may be misleading: they are more like practical ways of computing singular vectors of the transport equation rather than actual Llyapunov vectors.

Backward FTLE fields show contours that correspond reasonably well to the main structures such as filaments, fronts and spirals that appear in geophysical and biogeochemical tracer fields (Beron-Vera and Olascoaga, 2009; Shadden *et al.*, 2009; Olascoaga *et al.*, 2008; Olascoaga *et al.*, 2006). Figure 1.8 (top panels) shows the contours of the FTLE field (1.11) over Sea Surface Temperature (SST) (left panel) and Mixed Layer Phytoplankton (MLP) (right panel). The FTLE field is shown in the bottom panel.

FTLE are computed from a sequence of *mesoscale* (1/4°) time-dependent velocity fields filtered from a high-resolution (1/54°) idealised simulation of the North Atlantic Ocean (carried out by Lévy *et al.* (2009)). High resolution tracer fields SST and MLP come from the same simulation. Contours of FTLE matches quite well the main patterns in the corresponding SST and MLP fields of this simulation. Lapeyre (2002) shows that for a freely decaying 2D turbulence flow, the orientation of the gradient of a *passive* tracer converges to that of backward FTLVs. Such alignment properties have also been observed for realistic oceanic flows and tracers (d'Ovidio *et al.*, 2009*b*). Figure 1.9 (bottom panel) shows the orientations of the backward FTLV that correspond to the aforementioned FTLE contour field. Tracer gradients (left panel: SST; right panel: MLP) also show similar orientations. These two properties (pattern matching between tracer and FTLE scalar fields and tracer gradient orientation alignment with FTLV orientation) should be exploited in a Direct Image Assimilation framework. Furthermore, Beron-Vera *et al.* (2010, Beron-Vera (2010) showed, using real data, that these properties remain valid with a mesoscale advection, i.e. when the resolution of the velocity field — from which FTLE-V are computed — is much lower than the resolution of the observed tracer field. This behaviour was also mentioned using another Lagrangian tool (FSLE) by Lehahn *et al.* (2007, d'Ovidio *et al.* (2009*b*). Our synthetic data exhibit the same behaviour: FTLE field of Figure 1.8 is computed from a mesoscale 1/4° velocity field on the same high-resolution (1/54°) grid as that used to compute the SST and MLP fields. This feature is crucial from both a practical and physical point of view: first, velocity fields obtained from ocean global circulation models do not often provide more than mesoscale information, whereas tracer images contain submesoscale information; second, FTLE-V may be used to quantify and characterise the link between scales.

Titaud *et al.* (2011) suggest constructing observation operators using information

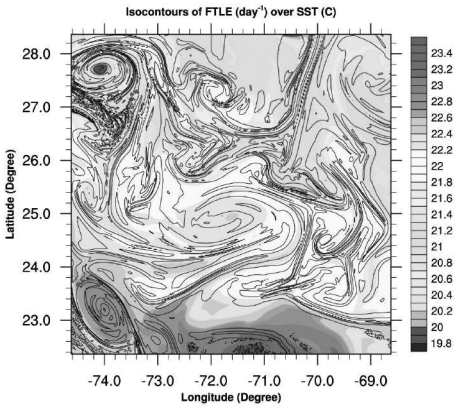

(a) Contours of FTLE over Sea Surface Temperature

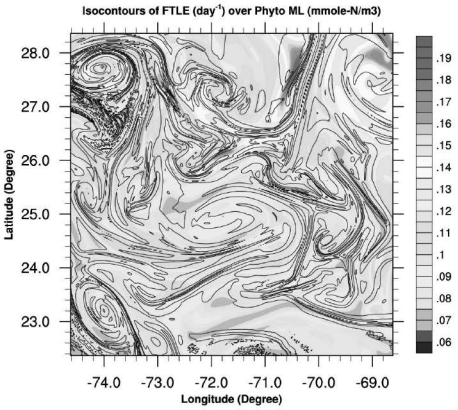

(b) Contours of FTLE Phytoplankton

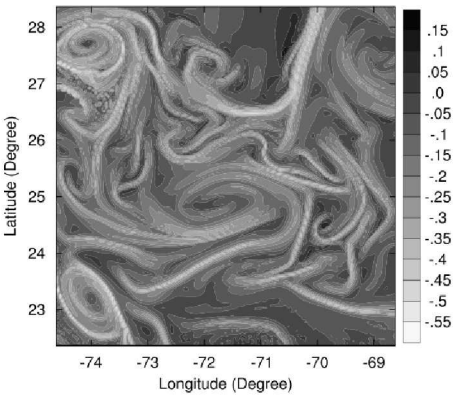

(c) Finite-Time Lyapunov Exponents field

Fig. 1.8 Contours of Finite-Time Lyapunov Exponents over Sea Surface Temperature and Mixed Layer phytoplancton. From a 1/54° North Atlantic Ocean simulation.

given by the computation of Lagrangian Coherent Structures. The main idea is to exploit the two aforementioned properties of the FTLE-V to construct a triplet of direct assimilation of images:

- FTLE: the observation space $\mathcal{I}$ is defined as a space of contours. Backward FTLE is viewed as an observation operator acting on the flow field $\mathbf{u}$ (subset of control variable) onto the image space $\mathcal{I}$:

$$\begin{aligned} \mathcal{H}[\mathbf{u}] : \Omega &\to \mathbb{R} \\ \mathbf{x} &\mapsto \sigma_{t_0}^{t_0+T}(\mathbf{x}). \end{aligned} \tag{1.12}$$

- FTLV: the observation space is the space of function on $\mathbb{R}^2$ with values in the Euclidean unit sphere equipped with an angular distance. The observation operator is simply the FTLV field:

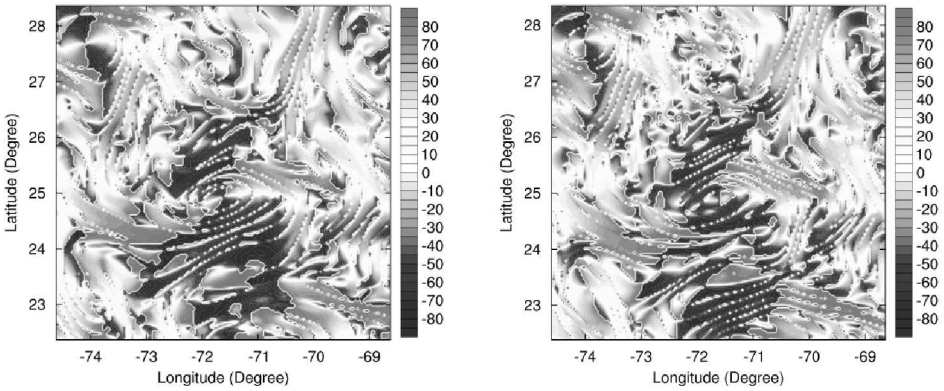

(a) Sea Surface Temperature, gradient orientation

(b) Phytoplankton, gradient orientation

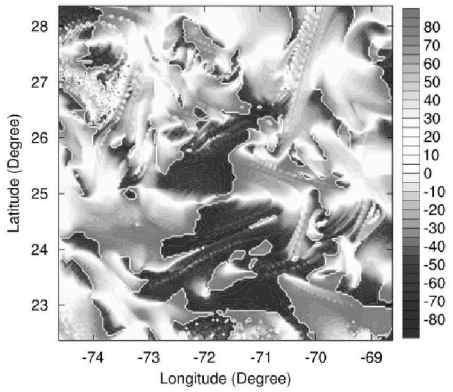

(c) Finite-Time Lyapunov Vectors orientations

Fig. 1.9 Orientations of Sea Surface Temperature and Mixed Layer phytoplancton gradient. Orientation of Finite-Time Lyapunov Vectors. From a 1/54° North Atlantic Ocean simulation.

$$\begin{aligned} \mathcal{H}[\mathbf{u}] : \Omega &\to \mathbb{R} \\ \mathbf{x} &\mapsto \varphi_{t_0}^{t_0+T}(\mathbf{x}). \end{aligned} \tag{1.13}$$

For the moment, few studies exist about the use of this kind of operator in direct image assimilation. In Titaud *et al.* (2011) a sensibility study proves the potential of this tool by showing that computation of FTLE-V is sensitive (in the direct image assimilation framework) to small perturbations of the velocity field. Figure 1.10 shows the variation of a sensitivity function (cost function) associated with the FTLE-V based observation operators with respect to the amplitude of nine random perturbations applied to a reference velocity field $\mathbf{u}$. Variations clearly have a minimum at the reference state and exhibit a convex shape that suggests a good situation for the inversion.

Even if not used in this description we also mention the Finite-Size Lyapunov

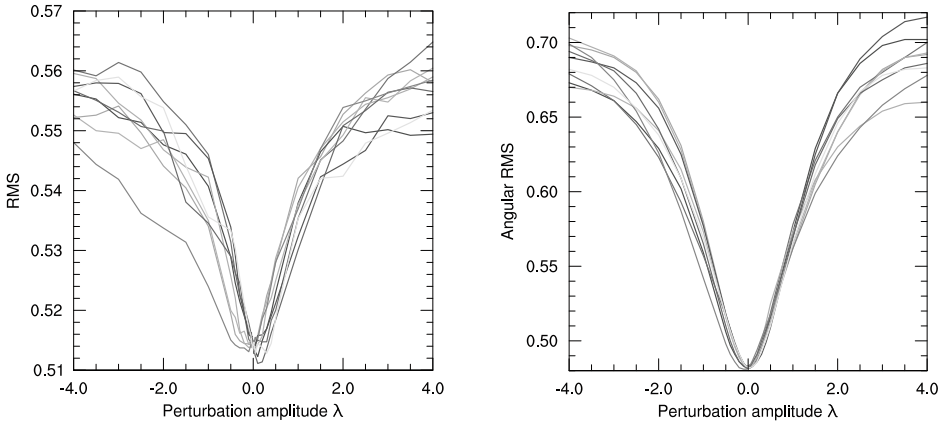

(a) SST: sensitivity of the FTLE-based observation operator

(b) SST: sensitivity of the FTLV-based observation operator

Fig. 1.10 Variation of a sensitivity function (cost function) associated with the FTLE-V based observation operators with respect to the amplitude of nine random perturbations applied to a reference velocity field $\mathbf{u}$.

Exponents (FSLE) (Aurell *et al.*, 1997; Artale *et al.*, 1997) which is another Lagrangian tool that is commonly used in oceanographic contexts for studying mixing processes (d'Ovidio *et al.*, 2004; d'Ovidio *et al.*, 2009*a*; d'Ovidio *et al.*, 2009*b*; Lehahn *et al.*, 2007, and references therein). In Gaultier *et al.* (2012) such FSLE field was used to reconstruct a ocean surface velocity field.

References

Adrian, Ronald J. (1991). Particle-imaging techniques for experimental fluid mechanics. *Annual review of fluid mechanics*, **23**(1), 261–304.

Amodei, L. and Benbourhim, M. N. (1991, October). A vector spline approximation. *J. Approx. Theory*, **67**(1), 1–29.

Artale, V, Boffetta, G, Celani, A, Cencini, M, and Vulpiani, A (1997). Dispersion of passive tracers in closed basins: Beyond the diffusion coefficient. *Phys. Fluids*, **9**(11), 3162–3171.

Aubert, Gilles and KornProbst, Pierre (2006, October). Mathematical Problems in Image Processing. Springer, New York.

Aurell, E, Boffetta, G, Crisanti, A, Paladin, G, and Vulpiani, A (1997). Predictability in the large: an extension of the concept of Lyapunov exponent. *Journal of Physics A: Mathematical and General*, **30**(1), 1–26.

Auroux, Didier and Fehrenbach, Jérôme (2010, July). Identification of velocity fields for geophysical fluids from a sequence of images. *Exp Fluids*, **50**(2), 313–328.

Beron-Vera, Francisco J (2010). Mixing by low- and high-resolution surface geostrophic currents. *J. Geophys. Res.*, **115**(C10027), 15pp.

Beron-Vera, Francisco J and Olascoaga, M J (2009). An Assessment of the Importance of Chaotic Stirring and Turbulent Mixing on the West Florida Shelf. *J. Phys. Oceanogr.*, **39**(7), 1743–1755.

Beron-Vera, Francisco J, Olascoaga, María J, and Goni, Gustavo J (2010, November). Surface Ocean Mixing Inferred from Different Multisatellite Altimetry Measurements. *J. Phys. Oceanogr.*, **40**(11), 2466–2480.

Bormann, N, Saarinen, S, and Kelly, G (2003). The spatial structure of observation errors in atmospheric motion vectors from geostationary satellite data. *Mon. Wea. Rev.*, **131**(4), 706–718.

Candès, Emmanuel and Donoho, David L (2003). New tight frames of curvelets and optimal representations of objects with piecewiseC2 singularities. *Comm. Pure Appl. Math.*, **57**(2), 219–266.

Chan, Tony F and Shen, Jianhong (2005). *Image processing and analysis*. variational, PDE, wavelet, and stochastic methods. SIAM, Philadelphia.

Corpetti, Thomas, Héas, Patrick, Memin, Étienne, and Papadakis, Nicolas (2009, January). Pressure image assimilation for atmospheric motion estimation. *Tellus A*, **61**(1), 160–178.

d'Ovidio, Francesco, Fernández, Vicente, Hernández-García, Emilio, and López, Cristóbal (2004). Mixing structures in the Mediterranean Sea from finite-size Lyapunov exponents. *Geophys. Res. Lett.*, **31**(L17203), 4pp.

d'Ovidio, Francesco, Isern-Fontanet, Jordi, López, Cristóbal, Hernández-García, Emilio, and García-Ladona, Emilio (2009*a*, January). Comparison between Eule-

rian diagnostics and finite-size Lyapunov exponents computed from altimetry in the Algerian basin. *Deep Sea Research Part I: Oceanographic Research Papers*, **56**(1), 15–31.

d'Ovidio, Francesco, Taillandier, V, Taupier-Letage, I, and Mortier, L (2009*b*, January). Lagrangian validation of the Mediterranean mean dynamic topography by extraction of tracer frontal structures. *Mercator Ocean Quarterly Newsletter*, **32**, 24–32.

Gaultier, Lucile, Verron, Jacques, Brankart, Jean-Michel, Titaud, Olivier, and Brasseur, Pierre (2012, March). On the inversion of submesoscale tracer fields to estimate the surface ocean circulation. *Journal of Marine Systems*, in press.

Geman, Stuart and Geman, Donald (1984, November). Stochastic Relaxation, Gibbs Distributions, and the Bayesian Restoration of Images. *IEEE Trans. Pattern Anal. Mach. Intell.*, **6**, 721–741.

Haben, S. A., Lawless, A S, and Nichols, N K (2011, July). Conditioning and preconditioning of the variational data assimilation problem. *Computers & Fluids*, **46**(1), 252–256.

Haller, Georges (2000). Finding finite-time invariant manifolds in two-dimensional velocity fields. *Chaos*, **10**(1), 99–108.

Haller, Georges (2001). Lagrangian structures and the rate of strain in a partition of two-dimensional turbulence. *Phys. Fluids*, **13**(11), 3365–3385.

Haller, Georges (2002). Lagrangian coherent structures from approximate velocity data. *Phys. Fluids*, **14**(6), 1851–1861.

Haller, Georges (2011, March). A variational theory of hyperbolic Lagrangian Coherent Structures. *Physica D*, **240**(7), 574–598.

Haller, Georges and Yuan, G (2000). Lagrangian coherent structures and mixing in two-dimensional turbulence. *Physica D: Nonlinear Phenomena*, **147**(3-4), 352–370.

Horn, Berthold K P and Schunck, Brian G (1981, August). Determining optical flow. *Artificial Intelligence*, **17**(1-3), 185–203.

Korotaev, G, Huot, E, Le Dimet, F, Herlin, Isabelle, Stanichny, S, Solovyev, D, and Wu, L (2008, April). Retrieving ocean surface current by 4-D variational assimilation of sea surface temperature images. *Remote Sensing of Environment*, **112**(4), 1464–1475.

Lapeyre, Guillaume (2002). Characterization of finite-time Lyapunov exponents and vectors in two-dimensional turbulence. *Chaos*, **12**(3), 688–11.

Lehahn, Y, d'Ovidio, Francesco, Lévy, M, and Heifetz, E (2007, August). Stirring of the northeast Atlantic spring bloom: A Lagrangian analysis based on multisatellite data. *J. Geophys. Res.*, **112**(C8), 15.

Lévy, Marina, Iovino, D, Masson, S, Madec, G, Klein, P, Tréguier, A M, and Takahashi, K (2009, October). Remote impacts of Sub-Mesoscale Dynamics on new production. *Mercator Ocean Quarterly Newsletter*, **13**, 13–17.

Mallat, Stéphane G (1998). *A wavelet tour of signal processing*. Morgan Kaufmann.

Mathur, Manikandan, Haller, Georges, Peacock, Thomas, Ruppert-Felsot, Jori E., and Swinney, Harry L. (2007, April). Uncovering the Lagrangian Skeleton of Turbulence. *Phys. Rev. Lett.*, **98**(14), 144502.

Michel, Yann (2011, February). Displacing Potential Vorticity Structures by the

Assimilation of Pseudo-Observations. *Mon. Wea. Rev.*, **139**(2), 549–565.

Michel, Y and Bouttier, F (2006, October). Automated tracking of dry intrusions on satellite water vapour imagery and model output. *Q.J.R. Meteorol. Soc.*, **132**(620), 2257–2276.

Nieman, S., MENzel, P., Hayden, C., Gray, D., Wanzong, S., Velden, C., and Daniels, J. (1997). WP Menzel, CM Hayden, D. Gray, ST Wanzong, CS Velden, and J. Daniels, 1997: Fully automated cloud-drift winds in NESDIS operations. *Bull. Amer. Meteor. Soc*, **78**, 1121–1133.

Olascoaga, M J, Beron-Vera, Francisco J, Brand, L E, and ak, H Ko c c (2008). Tracing the early development of harmful algal blooms on the West Florida Shelf with the aid of Lagrangian coherent structures. *J. Geophys. Res.*, **113**(C12014), 10 pp.

Olascoaga, M J, Rypina, I I, Brown, M G, Beron-Vera, Francisco J, ak, H Ko c c, Brand, L E, Halliwell, G R, and Shay, L K (2006). Persistent transport barrier on the West Florida Shelf. *Geophys. Res. Lett.*, **33**(L22603), 5pp.

Ott, Edward (1993). *Chaos in Dynamical Systems*. Chaos in Dynamical Systems. Cambridge University Press, New York, USA.

Ottino, J. M. (1989). The Kinematics of Mixing: Stretching, Chaos, and Transport . Cambridge University Press.

Papadakis, Nicolas and Memin, Étienne (2008). Variational Assimilation of Fluid Motion from Image Sequence. *SIAM J. on Imaging Sciences*, **1**(4), 343–363.

Schmetz, J., Holmlund, K., Hoffman, J., Strauss, B., Mason, B., Gaertner, V., Koch, A., and van DE, B. (1993). Operational cloud-motion winds from Meteosat infrared images. *Journal of applied meteorology*, **32**(7), 1206–1225.

Shadden, Shawn C, Lekien, Francois, and Marsden, Jerrold E (2005). Definition and properties of Lagrangian coherent structures from finite-time Lyapunov exponents in two-dimensional aperiodic flows. *Physica D: Nonlinear Phenomena*, **212**(3-4), 271–304.

Shadden, Shawn C, Lekien, Francois, Paduan, Jeffrey D, Chavez, Francisco P, and Marsden, Jerrold E (2009). The correlation between surface drifters and coherent structures based on high-frequency radar data in Monterey Bay. *Deep Sea Research Part II: Topical Studies in Oceanography*, **56**(3-5), 161–172.

Souopgui, Innocent (2010, November). *Assimilation d'images pour les fluides géophysiques*. Ph.D. thesis, Université de Grenoble et université de Yaoundé I.

Titaud, Olivier, Brankart, Jean-Michel, and Verron, Jacques (2011). On the use of Finite-Time Lyapunov Exponents and Vectors for direct assimilation of tracer images into ocean models. *Tellus A*, **63**(5), 1038–1051.

Titaud, Olivier, Vidard, Arthur, Souopgui, I, and Le Dimet, F.-X. (2010, January). Assimilation of image sequences in numerical models. *Tellus A*, **62**(1), 30–47.

Vigan, X, Provost, C, Bleck, R, and Courtier, P. (2000). Sea surface velocities from sea surface temperature image sequences 1. Method and validation using primitive equation model output. *J. Geophys. Res.*, **105**(C8), 19499–19514.

Wiggins, Stephen (1992). *Chaotic transport in dynamical systems*. Springer-Verlag, New York.